ROYAL SOCIETY OF CHEMISTRY

EDGE ARTICLE

Check for updates

SIM imaging of bacterial membrane dynamics and lipid peroxidation during photodynamic inactivation with a dual-functional activatable probe†

Yi Tao,[ab] Qinglong Qiao,*[a] Yiyan Ruan,[ab] Xiangning Fang,[ab] Xiang Wang,[a] Yinchan Zhang,[ab] Pengjun Bao,[ab] Yalin Huang[ab] and Zhaochao Xu [ORCID] *[ab]

Photodynamic inactivation (PDI) has emerged as a promising antibacterial strategy that mitigates the risk of bacterial resistance. However, the precise morphological dynamics and mechanisms underlying bacterial cell death during PDI remain insufficiently understood. In this study, we developed a dual-functional activatable probe, RDP, which integrated rhodamine B as a fluorophore with moderate brightness and fatty chains for selective bacterial membrane localization. The probe employed an aggregation-disaggregation mechanism to achieve both fluorescence activation and PDI functionality. Using super-resolution fluorescence imaging, we unveiled the selective rupture of bacterial membranes at specific sites during PDI, followed by membrane contraction and internalization, ultimately leading to the formation of lipid-enriched droplets within the bacteria. Further mechanistic investigations confirmed that this membrane rupture was driven by lipid peroxidation. Statistical analysis of bacterial morphological changes during PDI revealed that membrane rupture predominantly occurred at the septum during cell division, whereas in other growth phases, rupture sites were mainly localized at the poles. These findings provide critical insights into the role of selective membrane rupture in bacterial growth and viability, paving the way for the rational design of targeted and highly efficient antibacterial agents.

Introduction

The rise of antibiotic-resistant bacteria poses a critical global health challenge, necessitating the development of innovative antibacterial strategies.[1–4] Photodynamic inactivation (PDI) has emerged as a promising approach for eradicating pathogenic microorganisms, with applications in medicine and food safety.[5–11] PDI relies on light-activated photosensitizers (PSs) to generate reactive oxygen species (ROS), which oxidize bacterial cellular components, leading to cell death. This strategy exhibits broad-spectrum antibacterial activity, particularly against antibiotic-resistant bacteria.[12–15] Unlike conventional antibiotics, PDI induces bacterial membrane disruption through a non-specific, multi-targeted, and irreversible oxidative mechanism, simultaneously damaging other cellular structures. This significantly reduces the likelihood of resistance development, making PDI a promising alternative for

antimicrobial therapy.[16] However, the bactericidal mechanism of PDI is highly complex, involving multiple biochemical pathways and cellular responses.[17] A comprehensive understanding of these mechanisms remains incomplete, which hinders the rational design of PDI agents and their widespread application across various fields.

During PDI, PSs primarily target the bacterial plasma membrane or DNA, with the membrane being the primary site of damage and a key determinant of bacterial cell death.[18–20] The lipid components of the bacterial membrane play essential roles in nutrient exchange, intercellular communication, and structural integrity.[21–24] When ROS oxidize membrane lipids, the resulting structural disruption leads to loss of function and ultimately cell death.[25] Therefore, understanding the dynamic changes in the bacterial membrane during PDI is crucial for elucidating its bactericidal mechanism. While previous studies have largely focused on the overall antimicrobial effects of PDI, the detailed morphological and molecular-level changes in bacterial membranes remain poorly understood.[26–30] A thorough investigation of bacterial membrane dynamics during PDI would provide critical insights into its mechanism of action, facilitating the design of more effective PDI agents. However, the bacterial membrane is highly dynamic, primarily composed

[a]*Dalian Institute of Chemical Physics, Chinese Academy of Sciences, 457 Zhongshan Road, Dalian 116023, China. E-mail: qqlqiao@dicp.ac.cn; zcxu@dicp.ac.cn*

[b]*University of Chinese Academy of Sciences, Beijing 100049, China*

† Electronic supplementary information (ESI) available. See DOI: https://doi.org/10.1039/d5sc00858a

of phospholipids such as phosphatidylethanolamine (PE) and phosphatidylglycerol (PG), which assemble into nanoscale microdomains (2–200 nm) with distinct structural and functional properties.[31] Capturing these dynamic changes requires advanced imaging techniques capable of resolving nanoscale membrane structures in real time. Recent advances in super-resolution fluorescence microscopy have provided powerful tools for visualizing bacterial membranes, enabling the analysis of their structural and functional dynamics at nanometer resolution.[32–35] Therefore, developing probes that can image bacterial membranes with super-resolution during PDI is essential for elucidating the underlying mechanisms of bacterial cell death.

Despite this need, there remains a significant gap in the development of probes that integrate bacterial membrane imaging with PDI activity, enabling real-time, *in situ* visualization of membrane dynamics. Current PSs, while effective in bacterial eradication, often lack intrinsic fluorescence, requiring the use of separate fluorescent probes to monitor bacterial membrane changes.[29,36,37] This limitation prevents direct visualization of the specific sites of PS action. Although some dual-functional probes with both PDI and fluorescence imaging capabilities have been developed, they often suffer from weak fluorescence intensity or poor photostability, making them unsuitable for long-term, high-resolution imaging.[38–40] As a result, they fail to provide real-time insights into bacterial membrane dynamics during PDI-induced cell death. Addressing this limitation requires the development of robust dual-functional probes that simultaneously enable high-resolution imaging of bacterial membranes and efficient PDI, thereby facilitating a deeper understanding of membrane disruptions induced by photosensitizers during bacterial inactivation.

To address these challenges, we developed a rhodamine-derived dual-functional probe, **RDP**, which enables both fluorescence imaging of the plasma membrane in Gram-positive bacteria and photodynamic inactivation (PDI)-induced bacterial death (Fig. 1). Rhodamine B was chosen as the fluorophore

due to its optimal brightness for effective fluorescence imaging and its ability to undergo intersystem crossing, facilitating the generation of ROS.[41] To achieve selective membrane targeting, a long fatty acid chain was conjugated to rhodamine B, promoting the formation of fluorescence-quenched aggregates in aqueous solution. Upon disaggregation, **RDP** monomers anchor to the bacterial plasma membrane *via* hydrophobic interactions with membrane lipids and electrostatic interactions with membrane phospholipids, leading to fluorescence activation and localized ROS production. This ROS-mediated lipid peroxidation disrupts the membrane structure, ultimately causing bacterial cell death. Using **RDP**, we achieved real-time SIM imaging of bacterial membrane dynamics during PDI, capturing rupture events that drive lipid peroxidation-induced droplet formation. Super-resolution imaging further enabled us to construct a dynamic model of bacterial membrane behaviours during PDI, revealing that membrane rupture preferentially occurs at the septum during cell division and at the poles in other growth stages. This study advances our understanding of the molecular mechanisms underlying PDI and provides a foundation for the rational design of targeted antibacterial agents.

Results and discussion

Aggregation–disaggregation-induced fluorescence activation and ROS generation

To examine the fluorogenicity of **RDP** towards the bacterial membrane, the spectral properties of **RDP** in various solvents were first measured (Fig. 2a, b, and S1†). The quantum yield of **RDP** in PBS was found to be 0.02, accompanied by a broad absorption spectrum, indicating significant fluorescence quenching. However, in the presence of surfactants, the fluorescence intensity was dramatically enhanced, increasing by 156-fold and 139-fold in SDS and TritonX-100, respectively (Fig. 2b). Moreover, both the molar extinction coefficient (ε) and fluorescence quantum yield (Φ) showed significant improvements (Fig. 2c).

We hypothesized that the significant increase in fluorescence intensity of **RDP** in the presence of surfactants could be attributed to two main factors. The first factor is the fluorescence quenching effect due to aggregation. The long fatty acid chains facilitated the formation of **RDP** aggregates in aqueous solution, leading to fluorescence quenching. This was confirmed by comparing the absorption spectra, which showed a reduced absorbance of **RDP** in PBS, with an absorption peak at 558 nm corresponding to aggregates. Furthermore, dynamic light scattering (DLS) and fluorescence microscopy confirmed the formation of **RDP** aggregates in PBS (Fig. S2†). When the concentration of **RDP** in PBS reached 0.05 μM, aggregate particles began to form, with the particle size increasing gradually as the concentration of **RDP** was raised (Fig. S2a†). When the concentration of **RDP** was 5 μM, the DLS results revealed a relatively broad particle size distribution (polydispersity index, PDI = 0.307), indicating the coexistence of larger aggregate particles and smaller particles, with an average particle size of approximately 685.5 nm (Fig. 2d). The second factor is the
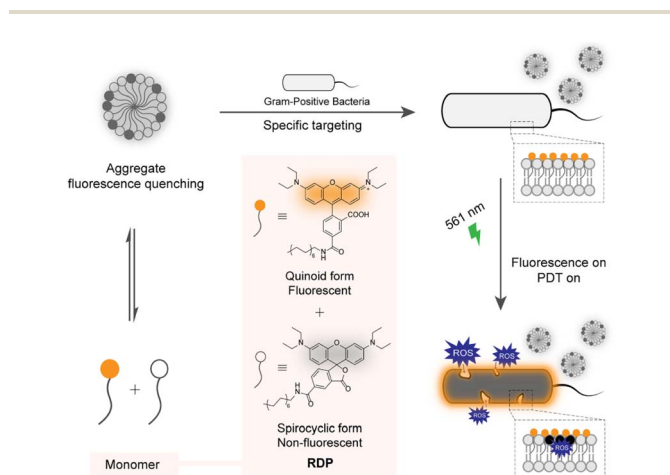

Fig. 1 Dual-functionality in super-resolution imaging and PDI *via* aggregation–disaggregation-induced activation of the photosensitizer RDP.
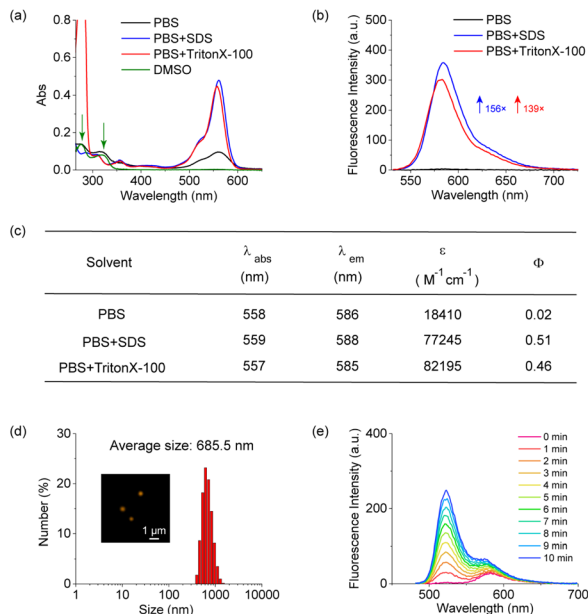
Fig. 2 The photophysical properties of **RDP**. (a) UV-Vis absorption spectra of **RDP** (5 µM) in PBS, PBS + SDS, PBS + TritonX-100, and DMSO. (b) Fluorescence emission spectra of **RDP** (5 µM) in PBS, PBS + SDS, and PBS + TritonX-100. $\lambda_{ex/em}$ = 520/590 nm. (c) Maximum absorption wavelength (λ_{abs}), maximum emission wavelength (λ_{em}), molar extinction coefficient (ε) and fluorescence quantum yield (Φ) of **RDP** in different solvents. (d) DLS analysis of **RDP** aggregates (5 µM) in PBS (PDI = 0.307), and fluorescence imaging of **RDP** aggregates (10 µM) in ultrapure water. (e) Fluorescence spectra of DCFH (2 µM) and **RDP** (2 µM) monomers in PBS + TritonX-100 solution after irradiation with 561 nm laser (40.6 mW cm^{-2}) for different time intervals. Excitation wavelength: 470 nm. Scale bar: 1 µm.

formation of non-fluorescent rhodamine spironolactone structures within the aggregates, which further contributed to the fluorescence quenching. This was evidenced by the absorption peaks at 275 nm and 321 nm, corresponding to spironolactone, which matched the absorption spectra observed in DMSO and indicated the presence of this non-fluorescent structure within the aggregates (Fig. 2a, green arrow). Additionally, **RDP** at various concentrations exhibited similar spectral characteristics, with the absorption spectra in PBS showing the characteristic absorption peak of the rhodamine spironolactone structure (Fig. S3†). The fluorescence quenching due to aggregation, along with the formation of non-fluorescent rhodamine spironolactone structures, led to a significant enhancement of fluorescence intensity upon the disaggregation of **RDP** aggregates into monomers. This suggested that **RDP** exhibited "fluorescence-on" properties, making it a promising candidate for bacterial wash-free fluorescence imaging applications.

Notably, the quantum yield of **RDP** in PBS with surfactants was approximately 0.5, suggesting the potential for intersystem crossing (ISC) to the triplet state (T_1), which could facilitate energy transfer to molecular oxygen, thereby promoting the generation of ROS. To evaluate ROS generation, we used dichlorofluorescein (DCFH), a fluorescent ROS probe, where ROS presence enhanced fluorescence at 525 nm.[42,43] Under 561 nm laser irradiation, DCFH fluorescence gradually

increased with **RDP**, but not with DCFH alone (Fig. 2e and S4†), confirming **RDP**'s ROS-generating capability. To identify the specific ROS generated by **RDP**, we first used ABDA to detect singlet oxygen ($^1O_2$). No change in ABDA absorbance at 380 nm indicated that **RDP** did not produce $^1O_2$ (Fig. S5†). We then used DCFH with quenchers VC (for $\cdot O_2^-$) and IPA (for $\cdot OH$) to detect the generation of $\cdot O_2^-$ and $\cdot OH$. A significant decrease in DCFH fluorescence with VC, but only a slight decrease with IPA, suggested that **RDP** primarily generated $\cdot O_2^-$ (Fig. S6†). Electron paramagnetic resonance (EPR) tests further confirmed $\cdot O_2^-$ generation (Fig. S7,† marked by blue dots), while other peaks, attributed to DMPO oxidation, did not interfere with $\cdot O_2^-$ detection. Therefore, the primary ROS generated by **RDP** was $\cdot O_2^-$, suggesting that **RDP** absorbed light energy, transitioned from the ground state (S_0) to the singlet state (S_1), and then underwent ISC to T_1. During the electron transfer process, the triplet state of **RDP** donated an electron to molecular oxygen, reducing it to $\cdot O_2^-$ (Type I reaction). These results also demonstrated that **RDP** could function as a dual-functional PS, capable of both imaging and PDI.

Fluorescence imaging of the plasma membrane of Gram-positive bacteria by RDP

Given the aggregation–disaggregation-induced fluorescence enhancement property of **RDP**, we investigated its potential as a fluorescent probe for wash-free imaging of living bacteria. We incubated five types of Gram-positive bacteria (*B. cereus*, *B. subtilis*, *S. aureus*, *S. epidermidis*, and *E. faecalis*) and three types of Gram-negative bacteria (*E. coli*, *C. freundii*, and *S. enteritidis*) with **RDP** and DAPI (a commercial nucleic acid dye) for 30 minutes, followed by wash-free confocal imaging. Gram-positive bacteria exhibited strong fluorescence on their membranes with a high signal-to-noise ratio (SNR, 7-fold), while Gram-negative bacteria showed negligible fluorescence (Fig. 3). This discrepancy can be attributed to the structural differences in the bacterial envelopes of Gram-positive and Gram-negative bacteria. In Gram-positive bacteria, the plasma membrane is surrounded by a thick peptidoglycan layer, allowing **RDP** to easily penetrate and reach the plasma membrane, where it anchored through electrostatic and hydrophobic interactions. In this environment, **RDP** initially formed non-fluorescent aggregates in bacterial solutions. However, upon targeting the membrane, the aggregates disaggregated into fluorescent rhodamine monomers, activating fluorescence and illuminating the plasma membrane of Gram-positive bacteria. In contrast, Gram-negative bacteria possess not only a thinner peptidoglycan layer but also an outer membrane rich in lipopolysaccharides, which hindered the entry of molecules and prevents **RDP** from reaching the plasma membrane. As a result, **RDP** effectively stained the plasma membrane of Gram-positive bacteria but not Gram-negative bacteria.

Photodynamic inactivation of Gram-positive bacteria using RDP

Meanwhile, we explored the potential of **RDP** as a photosensitizer for bacterial killing. We selected three common Gram-
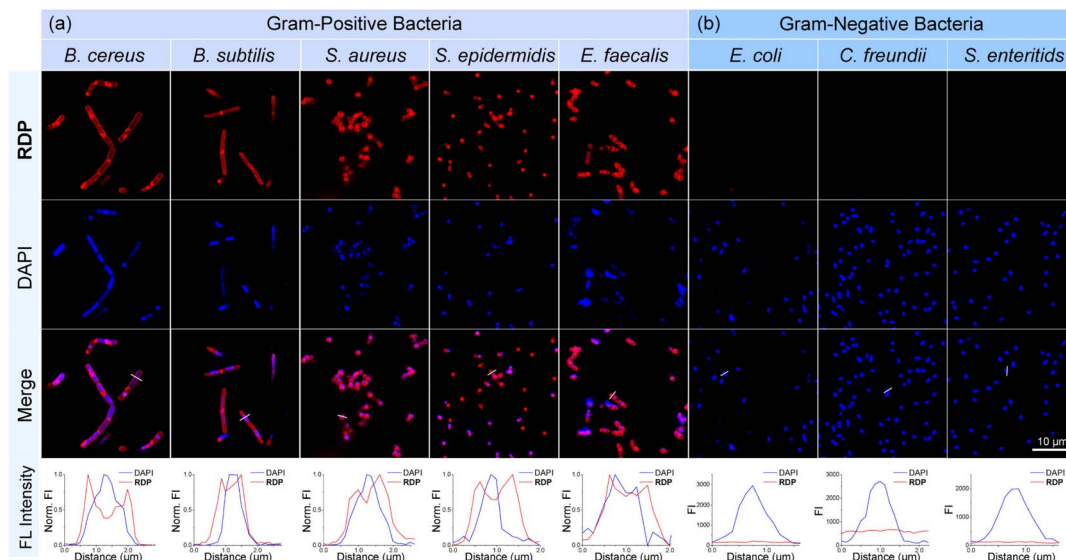
Fig. 3 Confocal fluorescence wash-free imaging of bacterial plasma membrane with **RDP**. (a) Five kinds of Gram-positive bacteria (*B. cereus, B. subtilis, S. aureus, S. epidermidis,* and *E. faecalis*) and (b) three kinds of Gram-negative bacteria (*E. coli, C. freundii,* and *S. enteritids*) (OD = 1) were pretreated with 2 μM **RDP** and 2 μM DAPI for 30 minutes, respectively, followed by fluorescence imaging (λ_{ex} = 405 nm/543 nm). And fluorescence intensity graphs normalized fluorescence profiles along the lines shown in merge images.

positive bacteria (*B. cereus*, *S. aureus*, and *E. faecalis*), one multidrug-resistant Gram-positive bacteria (*MDR S. aureus*), and one Gram-negative bacteria (*C. freundii*) to assess the bactericidal performance of **RDP**. The colony-forming unit (CFU) counting method was used to evaluate the photodynamic bactericidal effect. Bacteria labeled with different concentrations of **RDP** were exposed to 561 nm laser irradiation for 30 minutes, followed by incubation on solid culture plates at 37 °C. After 24 hours, colonies formed on the plates were counted and analyzed (Fig. 4). The results showed that for common Gram-positive bacteria (*B. cereus*, *S. aureus*, and *E. faecalis*), 90% of

the bacteria were eradicated at an **RDP** concentration of 0.625 μM (0.45 μg mL^{-1}) (Fig. 4a–c and f). For drug-resistant Gram-positive bacteria (*MDR S. aureus*), a higher **RDP** concentration of 1.25 μM (0.90 μg mL^{-1}) achieved a 99% kill rate (Fig. 4d and
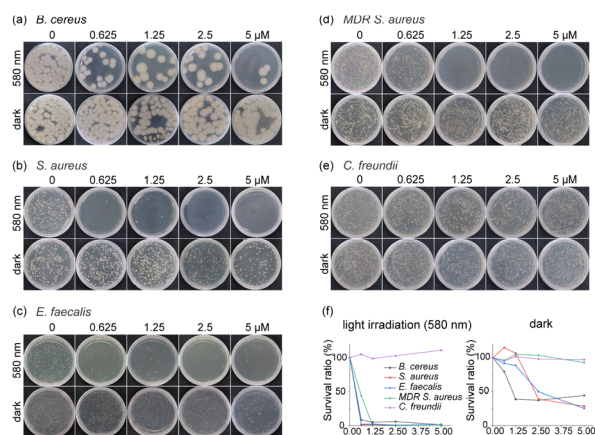

Fig. 4 Photodynamic antibacterial activity test results of **RDP**. (a) *B. cereus*, (b) *S. aureus*, (c) *E. faecalis*, (d) *MDR S. aureus* and (e) *C. freundii* were treated with different concentrations of **RDP** in dark/580 nm irradiation (5 mW cm^{-2}) for 30 min. Pictures of colony counting plates cultured 24 h in a 37 °C incubator. (f) Bacteria survival rates of different kinds of bacteria exposed to **RDP** (0–5 μM) in dark/580 nm irradiation (5 mW cm^{-2}).
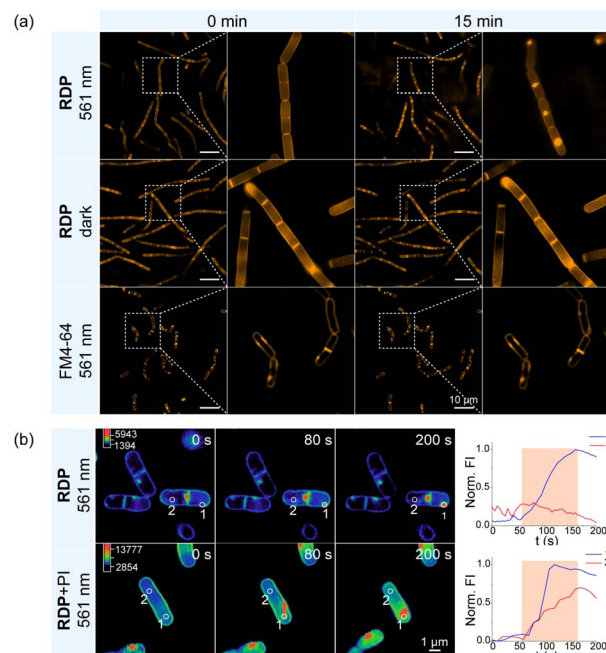

Fig. 5 SIM imaging and analysis of **RDP** photodynamic inactivation of *B. cereus*. (a) 0 and 15 min images of SIM imaging of *B. cereus* plasma membrane with **RDP** (2 μM, 30 min)/FM4-64 (5 μM, 30 min) in dark/ 561 nm irradiation. (b) Fluorescence intensity changes at different positions of long-term dynamic imaging of *B. cereus* treated with **RDP** (2 μM, incubation for 30 min)/**RDP** + PI (2 μM, incubation for 30 min). The orange area is an intensity mutation area.

f). In contrast, **RDP** exhibited negligible PDI activity against Gram-negative bacteria (Fig. 4e and f). These findings demonstrated the excellent PDI efficacy of **RDP** against Gram-positive bacteria. We speculated that once **RDP** anchored to the plasma membrane of Gram-positive bacteria, laser irradiation triggered ROS production, which disrupted the surrounding membrane structure and ultimately led to bacterial death. In contrast, **RDP** failed to kill Gram-negative bacteria due to its inability to penetrate and access their plasma membrane.

Leveraging the dual functionality of **RDP** to label the plasma membrane of Gram-positive bacteria and perform PDI, we utilized this probe to investigate the effects of PDI on bacterial plasma membrane using SIM super-resolution microscopy. *B. cereus* was stained with **RDP** and irradiated with a 561 nm laser for 15 minutes. A comparison of the imaging results before and after irradiation revealed a reduction in bacterial volume and the formation of spherical fluorescent bright spots inside the bacteria (Fig. 5a). In contrast, *B. cereus* stained with **RDP** in the dark or with FM4-64 (a commercial membrane dye) under 561 nm laser irradiation showed no observable changes (Fig. 5a

and S8). Based on these imaging results, we hypothesized that the reduction in bacterial volume and shrinkage of **RDP**-labeled bacteria under laser irradiation resulted from PDI, ultimately leading to bacterial death.

To further confirm bacterial death, we simultaneously labeled the bacteria with propidium iodide (PI), a commercial dye specific for marking dead bacteria. As a DNA dye, PI could not penetrate the intact cell membrane of live bacteria but readily entered through damaged membrane in dead bacteria to stain DNA, thereby distinguishing live and dead cells. *B. cereus* was stained with **RDP** alone and with a combination of **RDP** and PI, followed by 561 nm laser irradiation and imaging to monitor the formation of fluorescent bright spots within the bacteria. We extracted and analyzed the fluorescence spectra from regions where the bright spots appeared and other areas within the bacteria during this process (Fig. 5b). In the control group stained only with **RDP**, the fluorescence intensity of the bright spots increased, while no significant fluorescence enhancement was observed in other regions of the bacteria (Fig. 5b and Movie S1†). In contrast, in the experimental group stained with both
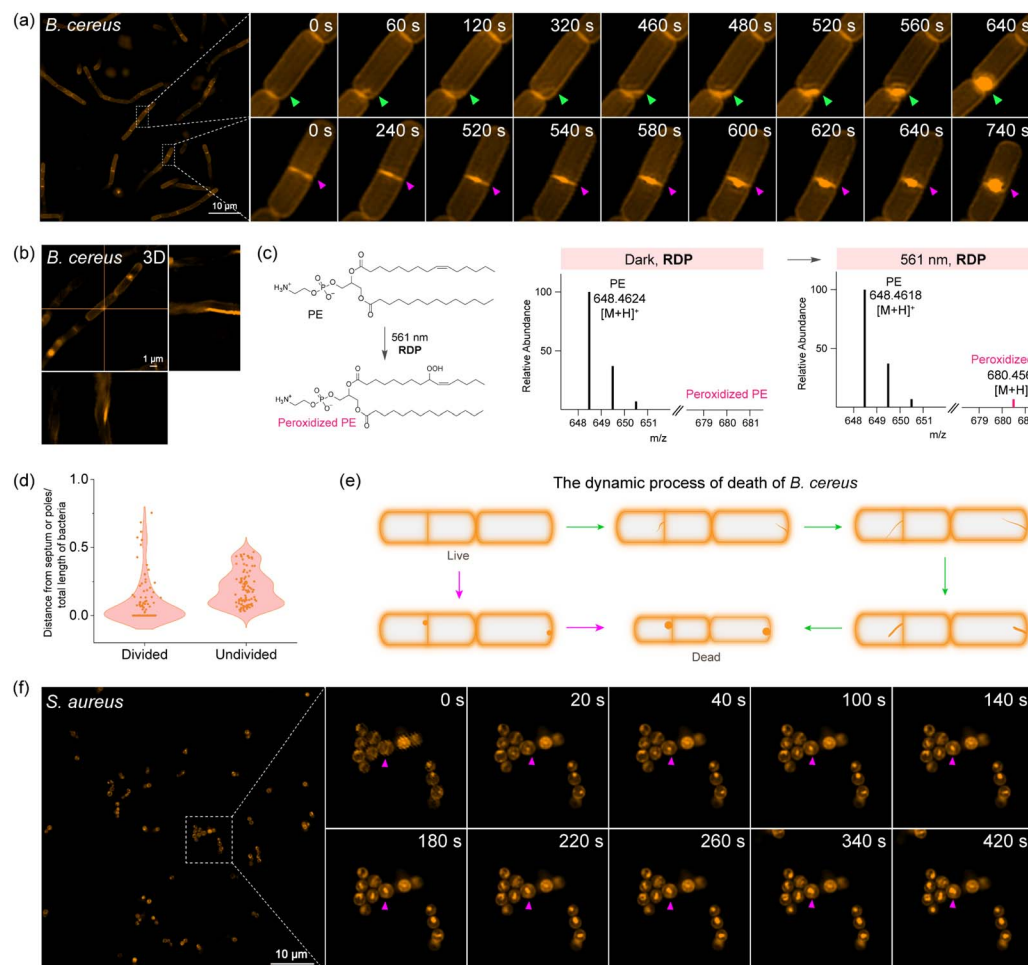

Fig. 6 Long-term SIM imaging of the plasma membrane during photodynamic inactivation of *B. cereus*. (a) *B. cereus* was pretreated with 2 μM **RDP** for 30 min, followed by SIM imaging and imaged for 15 min. (b) 3D images of dead *B. cereus* from different views. (c) Structure and HRMS analysis of PE and peroxidized PE on the plasma membrane of *B. cereus* before and after PDI. (d) The ratio of the distance between the fluorescent droplet and the septum or poles to the length of the bacterial cell. (e) Model of the dynamic death process of *B. cereus*. (f) *S. aureus* was pretreated with 2 μM **RDP** for 30 min, followed by SIM imaging and imaged for 15 min.

RDP and PI, the fluorescence intensity of other regions within the bacteria also showed a significant increase coinciding with the formation of the bright spots (Fig. 5b and Movie S2†). These results indicated that the generation of fluorescent bright spots corresponded to PDI-induced bacterial death, allowing PI to penetrate the damaged bacterial membrane and stain the DNA.

Imaging of plasma membrane dynamics during photodynamic inactivation of Gram-positive bacteria

To better understand the behavior of the bacterial plasma membrane during PDI, we used **RDP** to monitor the real-time dynamics of the plasma membrane in *B. cereus* (Fig. 6). During the ROS-induced bacterial death process, two distinct phenomena were observed on the plasma membrane: first, thin filaments appeared, which gradually thickened and condensed into bright spherical fluorescent spots, or second, small spherical fluorescent spots formed on the membrane and progressively grew into larger bright spots (Fig. 6a, Movie S3 and 4†). Three-dimensional structured illumination microscopy (3D-SIM) imaging confirmed that the spherical fluorescent spots were directly associated with the plasma membrane, forming on its surface (Fig. 6b). Simultaneously, bacterial shrinkage and a reduction in plasma membrane size were observed, coinciding with the formation of these fluorescent droplets. Based on these observations, we hypothesized that the fluorescent droplets were a result of membrane rupture, where damaged membrane lipids combined with fluorescent molecules. These damaged lipids likely consisted of lipid peroxides formed through ROS-induced lipid peroxidation driven by the PS.[44] To validate this hypothesis, membrane lipids from *B. cereus* were extracted before and after PDI and analyzed *via* high-resolution mass spectrometry, confirming damage and peroxidation, resulting in lipid peroxides (Fig. 6c and S9).[45]

Moreover, extensive super-resolution imaging allowed for detailed analysis of the locations where lipid-condensed droplets formed. For non-contracted, dividing bacteria, most droplets were located at the septum, whereas for contracted, non-dividing bacteria, droplet formation appeared more random, with a concentration near the poles (Fig. 6d). This suggested that the sites where lipid-condensed droplets formed corresponded to regions of membrane rupture. Statistical analysis indicated that ROS were more likely to target the bacterial plasma membrane near the septum and poles, areas potentially more vulnerable on the bacterial surface. Additionally, scanning electron microscopy (SEM) further demonstrated that bacterial membrane subjected to PDI exhibited rupture, particularly at the poles and septa, with leakage of intracellular contents from these sites (Fig. S10†). Based on these observations, we summarized the dynamic changes in the plasma membrane of *B. cereus* during PDI and proposed a model to describe this process (Fig. 6e). We concluded that two types of changes might occur on the plasma membrane: the first involves the appearance of filaments that transform into spherical fluorescent lipid droplets, and the second involves the growth of small spherical fluorescent droplets into larger ones. Both processes are more likely to occur near the septum and poles and are accompanied by gradual contraction and reduction of the plasma membrane's size.

Similar phenomena were also observed in *S. aureus*, where fluorescent lipid-condensed droplets predominantly formed at the septum of dividing bacteria (Fig. 6f and Movie S5†).

Conclusions

In conclusion, we have designed and synthesized an aggregation–disaggregation-regulated fluorescent probe, **RDP**, which selectively targeted the plasma membrane of Gram-positive bacteria through electrostatic and hydrophobic interactions, enabling effective fluorescence imaging. Additionally, **RDP** functioned as a photosensitizer (PS) for photodynamic inactivation (PDI), effectively inducing bacterial death through lipid peroxidation. By leveraging this dual-functionality, we developed a probe that both labels bacterial membranes for imaging and facilitates bacterial killing *via* PDI. Furthermore, we visualized the morphological changes in the plasma membrane of Gram-positive bacteria during cell death induced by lipid peroxidation. Our analysis highlighted that the regions most vulnerable to ROS attack were located near the septum and poles of the bacterial plasma membrane, which might represent key sites for bacterial inactivation. We believe this work provides valuable insights into the PDI bactericidal mechanism and holds promise for the development of new strategies for combating bacterial infections.

Data availability

All the data supporting this article have been included in the main text and the ESI.†

Author contributions

Y. Tao, Q. L. Qiao and Z. C. Xu conceived the methodology and supervised the project. Y. Tao, Y. Y. Ruan and X. Wang performed the biological experiments and statistical analyses. X. N. Fang, Y. C. Zhang, P. J. Bao and Y. L. Huang carried out the synthetic experimental work.

Conflicts of interest

There are no conflicts to declare.

Acknowledgements

Notes and references

1 J. L. Martínez, F. Baquero and D. I. Andersson, *Nat. Rev. Microbiol.*, 2007, **5**, 958–965.
2 E. M. Darby, E. Trampari, P. Siasat, M. S. Gaya, I. Alav, M. A. Webber and J. M. A. Blair, *Nat. Rev. Microbiol.*, 2022, **21**, 280–295.

3 D. Meziane-Cherif and P. Courvalin, *Nature*, 2014, **510**, 477–478.

4 E. D. Brown and G. D. Wright, *Nature*, 2016, **529**, 336–343.

5 S. M. Lashkari, H. Kariminezhad, H. Amani, P. Mataji and M. Rahimnejad, *Photodiagn. Photodyn. Ther.*, 2019, **25**, 336–343.

6 A. Späth, C. Leibl, F. Cieplik, K. Lehner, J. Regensburger, K.-A. Hiller, W. Bäumler, G. Schmalz and T. Maisch, *J. Med. Chem.*, 2014, **57**, 5157–5168.

7 M. Asnaashari, H. Homayuni and P. Paymanpour, *J. Lasers Med. Sci.*, 2016, **7**, 238–242.

8 V. S. Ghate, W. Zhou and H. G. Yuk, *Compr. Rev. Food Sci. Food Saf.*, 2019, **18**, 402–424.

9 Y. Liu, S. Wang, J. Wu, G. Qi, G. Chen, H. Li and H. Wang, *Food Bioprocess Technol.*, 2023, **17**, 1294–1308.

10 W. Dai, J. Hu, B. K. Tan and S. Lin, *Food Chem.*, 2025, **464**, 141925.

11 L. Chen, Y. Zhao, W. Wu, Q. Zeng and J. J. Wang, *Compr. Rev. Food Sci. Food Saf.*, 2023, **22**, 3814–3846.

12 J. F. Lovell, T. W. B. Liu, J. Chen and G. Zheng, *Chem. Rev.*, 2010, **5**, 2839–2857.

13 J. Sun, X. Cai, C. Wang, K. Du, W. Chen, F. Feng and S. Wang, *J. Am. Chem. Soc.*, 2021, **143**, 868–878.

14 W. Zhu, Y. Li, S. Guo, W.-J. Guo, T. Peng, H. Li, B. Liu, H.-Q. Peng and B. Z. Tang, *Nat. Commun.*, 2022, **13**, 7026.

15 X. Li, S. Lee and J. Yoon, *Chem. Soc. Rev.*, 2018, **47**, 1174–1188.

16 M. R. Hamblin and T. Hasan, *Photochem. Photobiol. Sci.*, 2004, **3**, 436–450.

17 T. Dai, Y.-Y. Huang and M. R. Hamblin, *Photodiagn. Photodyn. Ther.*, 2009, **6**, 170–188.

18 T. Maisch, R.-M. Szeimies, G. Jori and C. Abels, *Photochem. Photobiol. Sci.*, 2004, **3**, 907–917.

19 H. Ma, Y. Ma, L. Lei, W. Yin, Y. Yang, T. Wang, P. Yin, Z. Lei, M. Yang, Y. Qin and S. Zhang, *ACS Sustain. Chem. Eng.*, 2018, **6**, 15064–15071.

20 D. P. Valenzeno, *Photochem. Photobiol.*, 1987, **46**, 147–160.

21 H. Strahl and J. Errington, *Annu. Rev. Microbiol.*, 2017, **71**, 519–538.

22 L. M. Y. Mitchison-Field and B. J. Belin, *Curr. Opin. Microbiol.*, 2023, **74**, 102315.

23 I. Barák and K. Muchová, *Int. J. Mol. Sci.*, 2013, **14**, 4050–4065.

24 T.-Y. Lin and D. B. Weibel, *Appl. Microbiol. Biotechnol.*, 2016, **100**, 4255–4267.

25 E. Alves, T. Melo, C. Simões, M. A. F. Faustino, J. P. C. Tomé, M. G. P. M. S. Neves, J. A. S. Cavaleiro, Â. Cunha, N. C. M. Gomes, P. Domingues, M. R. M. Domingues and A. Almeida, *Rapid Commun. Mass Spectrom.*, 2013, **27**, 1607–1618.

26 X. Pang, D. Li, J. Zhu, J. Cheng and G. Liu, *Nano-Micro Lett.*, 2020, **12**, 144.

27 K. Li, Y.-Y. Zhang, G.-Y. Jiang, Y.-J. Hou, B.-W. Zhang, Q.-X. Zhou and X.-S. Wang, *Chem. Commun.*, 2015, **51**, 7923–7926.

28 J. Y. Hyun, C.-H. Lee, H. Lee, W.-D. Jang and I. Shin, *ACS Macro Lett.*, 2020, **9**, 1429–1432.

29 A. Tavares, C. M. B. Carvalho, M. A. Faustino, M. G. P. M. S. Neves, J. P. C. Tomé, A. C. Tomé, J. A. S. Cavaleiro, Â. Cunha, N. C. M. Gomes, E. Alves and A. Almeida, *Mar. Drugs*, 2010, **8**, 91–105.

30 J. Tang, B. Chu, J. Wang, B. Song, Y. Su, H. Wang and Y. He, *Nat. Commun.*, 2019, **10**, 4057.

31 G. Meer, D. R. Voelker and G. W. Feigenson, *Nat. Rev. Mol. Cell Biol.*, 2008, **9**, 112–124.

32 A. Carsten, M. Wolters and M. Aepfelbacher, *Mol. Microbiol.*, 2023, **121**, 646–658.

33 R. K. G. Tank, V. A. Lund, S. Kumar, R. D. Turner, L. Lafage, L. Pasquina Lemonche, P. A. Bullough, A. Cadby, S. J. Foster and J. K. Hobbs, *ACS Nano*, 2021, **15**, 16011–16018.

34 D. Jeong, M. J. Kim, Y. Park, J. Chung, H.-S. Kweon, N.-G. Kang, S. J. Hwang, S. H. Youn, B. K. Hwang and D. Kim, *BMC Biol.*, 2022, **20**, 270.

35 N. Pende, A. Sogues, D. Megrian, A. Sartori-Rupp, P. England, H. Palabikyan, S. K. M. R. Rittmann, M. Graña, A. M. Wehenkel, P. M. Alzari and S. Gribaldo, *Nat. Commun.*, 2021, **12**, 3214.

36 B. Mai, X. Wang, Q. Liu, A. W. Leung, X. Wang, C. Xu and P. Wang, *Lasers Surg. Med.*, 2016, **48**, 400–408.

37 L. Huang, M. Krayer, J. G. S. Roubil, Y.-Y. Huang, D. Holten, J. S. Lindsey and M. R. Hamblin, *J. Photochem. Photobiol., B*, 2014, **141**, 119–127.

38 H.-R. Jia, Y.-X. Zhu, Z. Chen and F.-G. Wu, *ACS Appl. Mater. Interfaces*, 2017, **9**, 15943–15951.

39 K. L. Smitten, H. M. Southam, J. B. de la Serna, M. R. Gill, P. J. Jarman, C. G. W. Smythe, R. K. Poole and J. A. Thomas, *ACS Nano*, 2019, **13**, 5133–5146.

40 E. Lee, X. Li, J. Oh, N. Kwon, G. Kim, D. Kim and J. Yoon, *Chem. Sci.*, 2020, **11**, 5735–5739.

41 L. Li, Y. Chen, W. Chen, Y. Tan, H. Chen and J. Yin, *Chin. Chem. Lett.*, 2019, **30**, 1689–1703.

42 M. D. J. F. Curtin and T. G. Cotter, *J. Immunol. Methods*, 2002, **265**, 49–72.

43 J. Yu, C.-H. Hsu, C.-C. Huang and P.-Y. Chang, *ACS Appl. Mater. Interfaces*, 2014, **7**, 432–441.

44 P. S. H. Wilker Caetano, R. Itri, D. Severino, V. C. Vieira, M. S. Baptista, A. ´P. Schröder and C. M. Marques, *Langmuir*, 2007, **23**, 1307–1314.

45 M. L. Y. N. A. Busch and M. Toner, *Biophys. J.*, 1998, **75**, 2956–2970.